

1 Optimizing the precision of infrared measurements using the Eppley 2 Laboratory, Inc. model PIR pyrgeometer

3
4
5 **Joseph J. Michalsky¹, John A. Augustine¹, Emiel Hall¹, and Benjamin R. Sheffer^{1, 2}**

6
7 ¹Global Monitoring Laboratory, National Oceanic and Atmospheric Administration,
8 Boulder, Colorado 80305, USA

9 ²Cooperative Institute for Research in Environmental Sciences, University of Colorado,
10 Boulder, Colorado 80309, USA

11
12 **Correspondence:** Joseph Michalsky (joseph.michalsky@noaa.gov)

13
14 **Abstract.** The Eppley Precision Infrared Radiometer (PIR) is widely used for broadband (3.5-50
15 μm), thermal infrared wavelength measurements of the downwelling and upwelling radiation
16 from the atmosphere and surface, respectively. The field of view of the instrument is 2π
17 steradians with a receiver that has an approximate cosine response. In this paper we examine four
18 equations suggested by the literature that have been used to transfer irradiance calibrations from
19 our standard PIRs that are calibrated at the World Radiation Center to field units used for
20 network operations. We first discuss various equations used to convert the resistance
21 measurements of the thermistors to temperatures of the body and dome that are used in the
22 derivation of incoming irradiance. We then use the four related, but distinct, equations for the
23 transfer of the calibration from standard PIRs to field instruments. A clear choice for the
24 preferred equation to use for calibration and transfer of calibration to field PIRs emerges from
25 this study.

26 27 28 **1. Introduction**

29
30 The Eppley Precision Infrared Radiometer (PIR) is a pyrgeometer developed to measure
31 broadband (3.5-50 μm) thermal infrared (hereafter, IR) radiation emitted by the atmosphere and
32 surface. Detecting even small changes in atmospheric and surface IR in the environment are
33 important to understand as they may indicate temperature changes in the environment caused by
34 changes in the atmospheric composition or cloud cover.

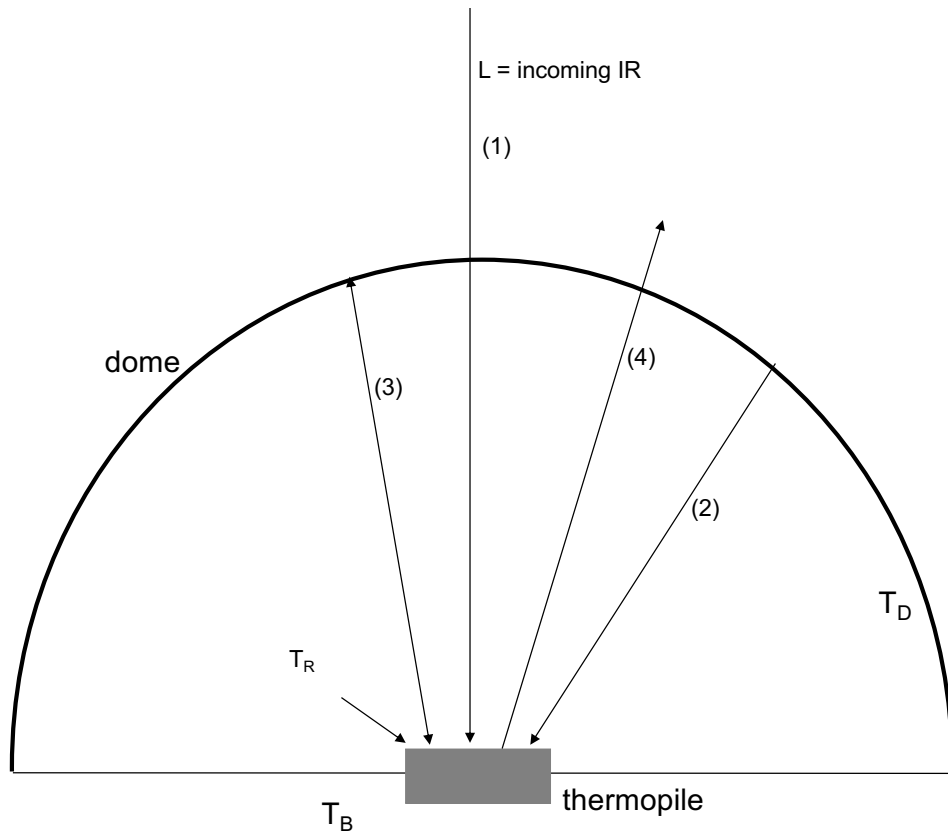
35
36 The PIR originally came equipped with a battery-powered circuit to compensate for the radiation
37 emitted by the body so the net signal from the instrument was a measure of actual incoming IR
38 radiation. Users of this instrument that are interested in the optimum precision in their IR
39 measurements do not use the battery-powered circuit, but, instead, use temperatures from two
40 thermistors connected to the body and dome of the instrument along with the thermopile output
41 to calculate the incoming IR irradiance signal.

42
43 Fig. 1 illustrates the most significant incoming and outgoing IR irradiances at the thermopile
44 surface. To derive L , the incoming IR radiation from the hemisphere outside the instrument,

45 radiative equilibrium of the instrument must be defined. To do that, the sum of the incoming
 46 radiation transmitted by the dome (labeled 1), radiation emitted by the dome to the receiver
 47 (labeled 2), and the radiation emitted by the thermopile surface and reflected by the dome
 48 (labeled 3) are set equal to the radiation emitted by the thermopile surface (labeled 4, which is
 49 the largest of the IR signals). Note that the dome transmits IR radiation between 3.5 and 50 μm ,
 50 however, the transmission is not perfect, nor uniform. Considering these components Albrecht
 51 and Cox (1977) formulated Eq. (1) for the externally received radiation as
 52

$$L = U_{thermopile}(c_1 + c_2 T_B^3) + \epsilon_o \sigma T_B^4 - k\sigma(T_D^4 - T_B^4), \quad (1)$$

53 where $U_{thermopile}$ is the voltage measured across the thermopile, T_B and T_D are the body and dome
 54 temperatures in K, σ is the Stefan-Boltzmann constant, ϵ_o is the emissivity of the detector, and
 55 c_1 , c_2 , and k are constants to be determined in calibration.
 56



57 **Figure 1.** Schematic for the most significant incoming and outgoing IR radiation components on
 58 the thermopile surface (numbered 1 – 4) that are considered in calculating the incident
 59 atmospheric IR irradiance. The top of the dark rectangle is the receiving surface surrounded by
 60 the dome that transmits IR in the range 3-50 μm . YSI 44031 thermistors are used to measure T_B
 61 of the body (thermistor buried in the brass body of the PIR) and T_D of the dome in K. T_R is the
 62 estimated receiver temperature in K.
 63
 64

65 In practice Albrecht and Cox (1977) dropped the $c_2 T_B^3$ term as negligible relative to the c_1 term
 66 and set the emissivity of the body of the instrument ϵ_0 to 1 yielding this commonly expressed
 67 form of their equation
 68

$$L = \frac{U_{thermopile}}{C} + \sigma T_B^4 - k\sigma(T_D^4 - T_B^4), \quad (2)$$

69
 70
 71 where c_1 has been replaced by $1/C$.

72
 73 Philipona et al. (1995), however, used Eq. (1) in its entirety, but to compare symbolically to Eq.
 74 (2) it is written
 75

$$L = \frac{U_{thermopile}}{C} (1 + k_1 \sigma T_B^3) + k_2 \sigma T_B^4 - k_3 \sigma (T_D^4 - T_B^4), \quad (3)$$

76
 77 where the T_B^3 term in Eq. (1) is retained, the emissivity of the body is k_2 , and k_3 is the same as k
 78 in Eq. (2). All constants, C , k_1 , k_2 , and k_3 , are determined in calibration.
 79
 80

81 Payne and Anderson (1999) used the functional form of Eq. (2), but substituted T_R for the T_B ,
 82 where T_R is the empirically calculated approximate temperature of the receiving surface rather
 83 than the measured body temperature as illustrated in Fig. 1. Thus,
 84

$$L = \frac{U_{thermopile}}{C} + \sigma T_R^4 - k\sigma(T_D^4 - T_R^4). \quad (4)$$

85
 86 Payne and Anderson (1999) estimated T_R using Eq. 5
 87

$$T_R = T_B + 0.694 \cdot U_{thermopile} \quad (5)$$

88
 89 where $U_{thermopile}$ is in millivolts, and the emissivity ϵ_0 is set to unity.
 90

91 Reda et al. (2002) used a form similar to Eq. (4)
 92

$$L = k_0 + \frac{U_{thermopile}}{C} + k_2 \sigma T_R^4 - k_3 \sigma (T_D^4 - T_R^4), \quad (6)$$

93
 94 where the instrument body emissivity k_2 is derived during calibration and a constant term k_0 is
 95 introduced. T_R is nearly the same as Eq. (5) with 0.704 replacing the constant 0.694. In this paper
 96 we drop the constant term k_0 since there is no physical justification for including it.
 97

98 Since there are four versions of the original Albrecht and Cox (1977) Eq. (1), this paper attempts
 99 to determine which version is best, in the precision sense, to use for the PIR calibration transfer.
 100 The organization of this paper is as follows. Because accurate internal thermistor temperatures
 101 are critical to pyrgeometer IR measurements, we first examine various versions of the standard

102 cubic equation used to convert the YSI 44031 thermistor resistance to the temperatures of the
 103 PIR body and dome. We then calibrate six test PIRs by transferring the calibrations of our three
 104 standard PIRs that were in turn calibrated at the World Radiation Center (WRC) in Davos,
 105 Switzerland, using the World Infrared Standard Group (WISG). Comparisons are then made
 106 between the mean irradiance of the three standard PIRs and the computed irradiance from the
 107 test PIRs using the four different forms of the original Albrecht and Cox (1977) formula, i.e., Eq.
 108 (1) to calibrate each. Boxplots are used to demonstrate the level of agreement between the
 109 standard PIRs and test PIRs for the various formulations. Lastly, a clear conclusion with regards
 110 to the preferred technique to use for calibrations and field measurements is suggested.

111
 112

113 2. PIR Temperature Measurements

114

115 The body and dome temperatures in the Eppley PIR pyrgeometer are measured using the YSI
 116 44031 thermistor. The YSI company provided a table of resistance versus temperature at one K
 117 resolution. To get a finer resolution, a mathematical fit to the tabulated data is required. Steinhart
 118 and Hart (1968) found that a cubic fit of inverse temperature to the log of measured resistance
 119 matched many of the manufacturer’s thermistor data points over a wide temperature range. Their
 120 equation is

121

$$\frac{1}{T} = a + b \cdot \ln(R) + c \cdot (\ln R)^2 + d \cdot (\ln R)^3, \quad (7)$$

122

123 where T is the temperature in K and R is the measured resistance in ohms or kilohms. Note that
 124 in the standard Steinhart-Hart equation, the ‘c’ is set to zero. Coefficients *a*, *b*, and *d* differ
 125 depending on whether ohms or kilohms are used, and on the temperature range over which the
 126 fit is made.

127

128 Fig. 2 is a plot of six independently-derived fits to the same manufacturer’s YSI 44031
 129 thermistor data, and the table below lists the coefficients of Eq. 7 for those fits. The y-axis is the
 130 temperature estimate based on the fit minus the tabulated thermistor data to which the fit is
 131 made. The least-squares fit to Eq. (7) (no quadratic term) is indicated by the red line if ohms are
 132 used. If a full cubic relationship, including a quadratic term, is used to fit the tabulated data in
 133 kilohms, then similar, but not identical, agreement to the red line is obtained (blue-white line).
 134 Interestingly, fitting the full cubic relationship to either ohms or kilohms yields identical results
 135 (again, note the blue-white line). This is not the case if the quadratic term is not included in the
 136 fitting to ohms versus kilohms as discussed in the appendix. Two gray fits in Fig. 2 are from the
 137 Baseline Surface Radiation Network (BSRN) - Operation Manual Version 2.1 (McArthur, 2005),
 138 and use YSI 44031 resistance in ohms. That published equation yields the bottom gray curve that
 139 is displaced from the main grouping in Figure 2. If their coefficient *a* is modified slightly from
 140 the published 0.0010295 to 0.0010293, as shown in the legend, then an improved fit (upper gray
 141 curve) is obtained that agrees well with the others. The green curve, used by the World Radiation
 142 Center (WRC) in Davos, Switzerland, was fit over a -30 to +40 °C range, but does well over the
 143 entire range of -50 to 50 °C considered here. Differences among the various fits in Fig. 2 are
 144 small. All but the bottom gray fit in Fig. 2 cause less than 0.1 Wm⁻² of uncertainty in the
 145 irradiance estimate.

146

	a =	b =	c =	d =
Red (ohms)	0.001029607	0.0002390769	0.0	1.567609E-07
White (ohms)	0.001020630	0.0002416721	-2.47485E-07	1.64547E-07
Blue (kiloohms)	0.002732470	0.0002618082	3.162474E-06	1.645474E-07
Gray (ohms)	0.0010295 Better 0.0010293	0.0002391	0.0	1.568E-07
Magenta (ohms)	0.00102972	0.00023906	0.0	1.5677E-07

147

148

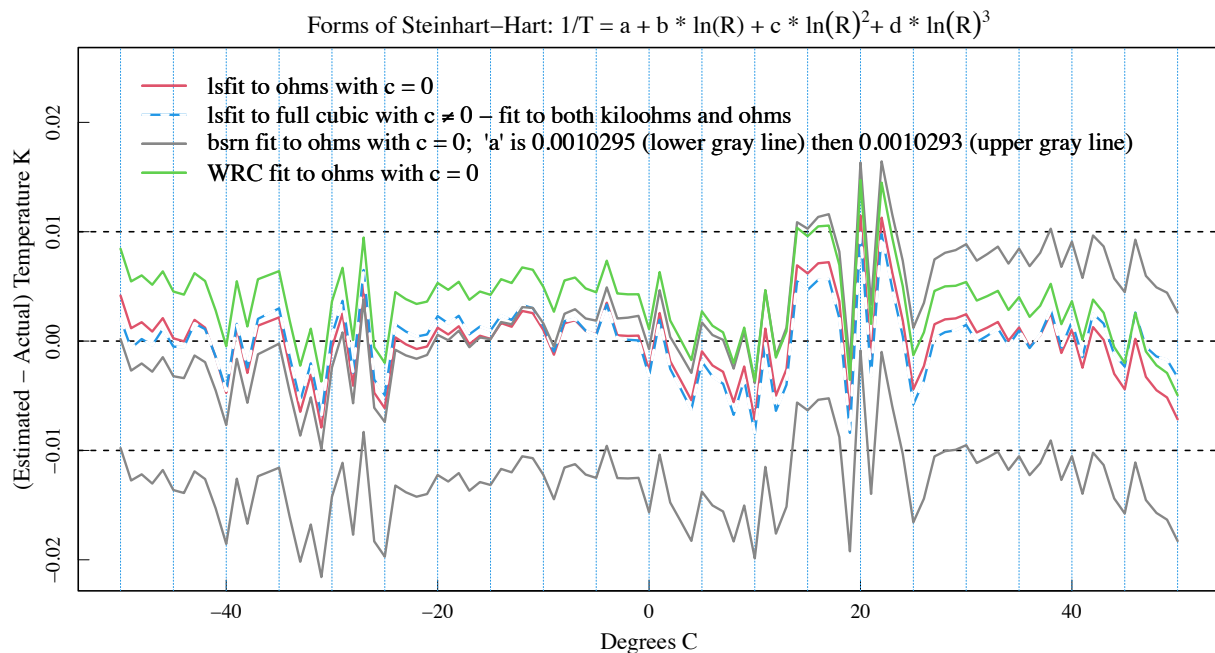
149

150

151

152

The larger uncertainty in thermistor temperature measurements is the fundamental accuracy of the thermistors used in the PIR, which are specified to be replaceable to 0.2 K. At 300 K, a difference of 0.2 K is a little over 1Wm^{-2} . In this paper the full cubic (blue-white curve) is used to compute PIR temperatures in the analyzed data.



153

154

155

156

157

158

159

160

161

Figure 2. Six independent fits using forms of Eq. (7) to the YSI 44031 tabulated data after subtraction of the tabulated data over the range -50 to 50 °C in 1 °C increments. Similar agreement among all fits ensues if the small change to the published BSRN constant a is made. The full cubic fits overlap whether ohms or kiloohms are used (with different coefficients, of course).

3. Four Methods of PIR Calibration Transfer

162

163

164

165

166

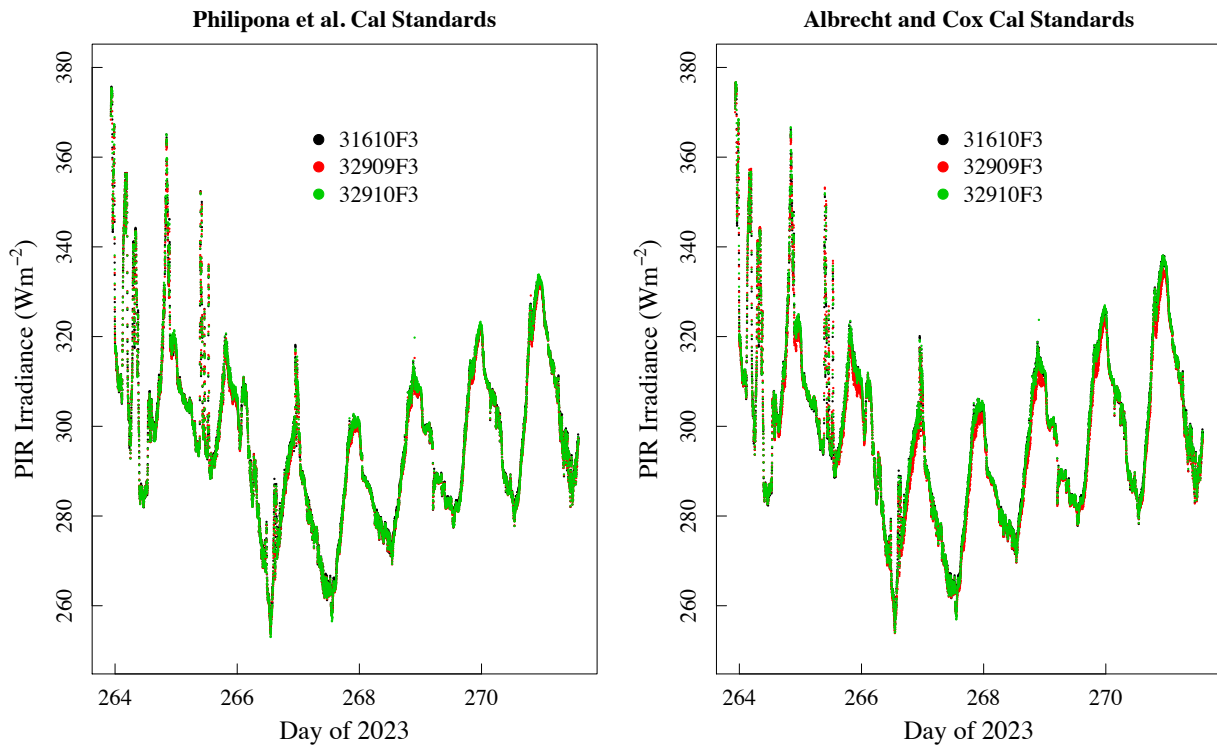
167

In this section, we examine the performance of Eq. (2), (3), (4), and (6) in transferring calibrations from our three “standard” PIRs to field PIRs. Our standard PIRs were calibrated against the world reference at the WRC (<https://www.pmodwrc.ch/en/world-radiation-center-2/irs/wisg/>) in 2018, 2022, and 2024 at the WRC, which is part of the PMOD in Davos, Switzerland. Each standard was returned with two sets of coefficients, one set for Eq. (2) and one set for Eq. (3). The WRC calibration of our standard PIRs uses their blackbody over a range of

168 pyrgeometer and cavity temperatures to determine the k_i 's in Eq. (3). The C determined by this
169 regression is not used, but is set using clear and stable skies outdoors.

170
171 To transfer the standard PIRs' calibration to field radiometers, our WRC-calibrated standard
172 PIRs and test PIRs are arranged side-by-side for a week or more on an outdoor horizontal
173 observing platform, with no significant obstructions surrounding the platform. Note that all
174 calibration coefficients of Eq. (3) for our test PIRs are obtained by regression analysis, i.e., we
175 used no blackbody for calibration transfer. For this paper two calibration periods and three PIRs
176 from each are analyzed. However, all figures for this paper only display results from the 2023
177 calibration performed at Table Mountain near Boulder, Colorado USA. Diurnal variability
178 shown in Fig. 3(a) indicates the type of conditions used for calibration. On the left are the three
179 standard PIR's outputs with the WRC's Philipona et al. (1995) coefficients applied. On the right
180 are the same standard PIR's with the WRC's Albrecht and Cox (1977) coefficients applied.
181 Agreement among the three on the left is very good because the last-plotted PIR readings (green)
182 overplot the first two (black and red). Agreement on the right is nearly as good but with some
183 underestimation by PIR 32909F3 (red dots). Histograms in Fig. 3(b) indicates the degree of
184 agreement among our standard PIRs more clearly with closer agreement among the results using
185 the Philipona et al. (1995) coefficients.

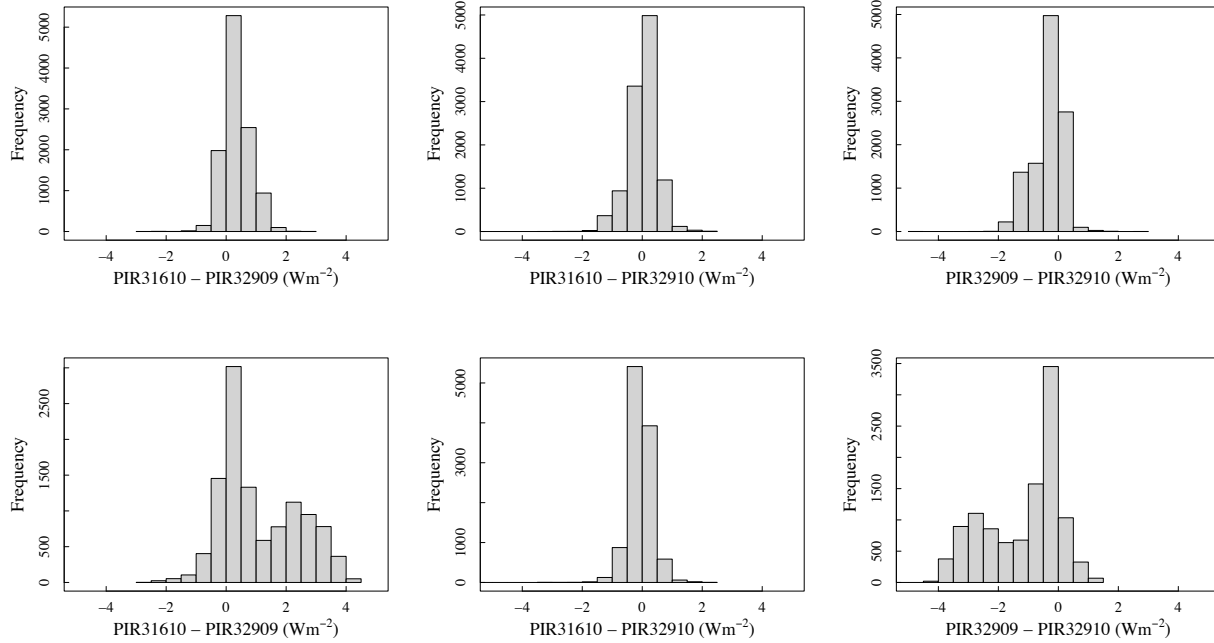
186



187
188 **Figure 3(a).** Calculated IR irradiance from our three standard PIRs (serial numbers in the
189 legend) using Philipona et al. coefficients provided by WRC are overplotted on the left and the
190 Albrecht and Cox coefficients are used on the right. This demonstrates the agreement among the
191 standard PIRs using the two methods. The number of days used is typical for our calibration
192 runs.

193

Figure 3 2023 Cal Run Using WRC Philipona et al. Coefs (top) and Albrecht and Cox Coefs (bottom) for Standards



194
 195 **Figure 3(b).** Histograms of the differences (Wm^{-2}) among our standard PIRs applying either the
 196 Philipona et al. (1995) WRC-assigned calibration coefficients (top) or the Albrecht and Cox
 197 (1997) WRC-assigned coefficients (bottom). Clearly, there is closer agreement in top row.
 198

199 Before comparing results from Eq. (2), (3), (4), and (6), we first compare results from only
 200 Albrecht and Cox (Eq. 2) and Philipona et al. (Eq. 3) for which the WRC provided both sets of
 201 coefficients. In this test, the mean IR irradiance of the three standard PIRs is compared to
 202 computed IR from a test PIR that was calibrated using the mean of these standard PIRs. The
 203 least-squares fitting technique to determine the calibration coefficients for the test instrument
 204 uses a robust function in the R language (MASS::rlm) that de-weights outliers to reduce the
 205 effects of noisy, for example, rain-contaminated, and other outlier data. As we shall discuss in
 206 the final section, this appears to be comparable to the strict criteria used at the WRC for
 207 calibration transfer. However, it should be noted that days with known rain events are removed
 208 from all test data sets before a calibration transfer is attempted.
 209

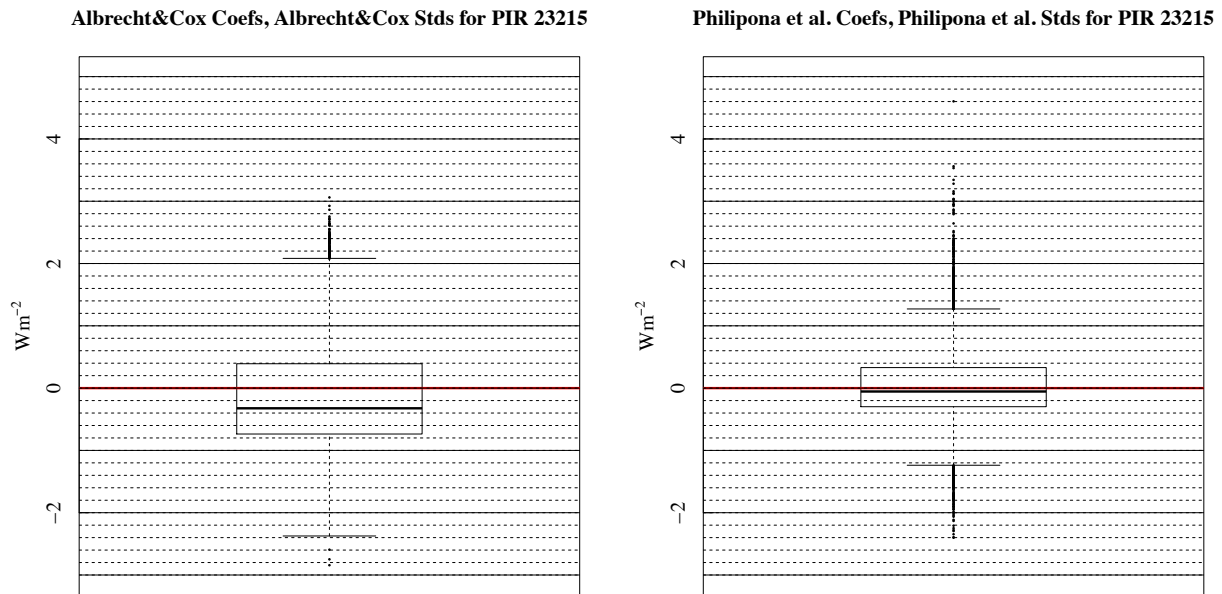
210 In Figure 4, boxplots are used to compare the performance of the two calibration methods
 211 applied to the standard PIRs at the WRC, i.e., Albrecht-and-Cox (1977) and Philipona et al.
 212 (1995). The “box” in these plots contain 50% of the data, and the lines extending from the top
 213 and bottom of the box, or “whiskers,” include about 95% for normally distributed data. In the
 214 top-left panel of Fig. 4 the three standard PIRs use the WRC-provided Albrecht and Cox (1977)
 215 coefficients, and the average of the three standard PIRs is compared to coincident test PIR (SN
 216 23215F3) data, also calculated using Albrecht and Cox (1977). The boxplot summarizes those
 217 differences over the entire calibration period for PIR 23215F3. The boxplot on the top right
 218 summarizes differences following the same procedure, but using Philipona et al. (1995)
 219 coefficients for the standard PIRs (WRC-provided) and for the test PIR. Comparing the top
 220 panels of Fig. 4, the one on the right, where Philipona coefficients are used exclusively, has a

221 smaller box, shorter whiskers, and a median nearer to zero compared to the panel on the left
222 where Albrecht and Cox was used exclusively.

223

224 The bottom panels of Fig. 4 show the same comparison for a different test PIR (SN 38805F3).
225 The same comments apply, with the Philipona et al. (1995) calibrated data (bottom right) giving
226 smaller spread in the box and whiskers, and the median nearer zero, while there is more spread in
227 the bottom-left panel where Albrecht and Cox (1977) is used. Differences in the lower panels of
228 Fig. 4 are generally greater than those in the top panels. The calibration data for these two test
229 instruments were collected concurrently, which suggests that the disparity arises from inherent
230 characteristics of the instruments themselves. We studied a total of six instruments from two
231 distinct calibration periods in this way and found that in every case using the Philipona et al.
232 (1995) form (Eq. 3) gave better results than the formulation of Albrecht and Cox (1977) (Eq.
233 (2)).

234

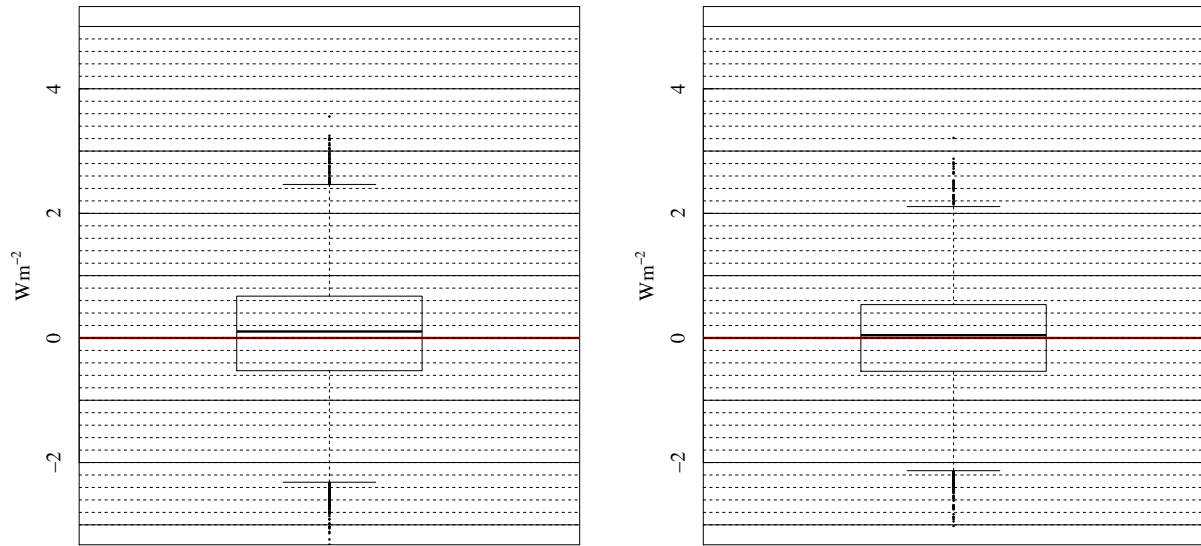


235

236

Albrecht&Cox Coefs, Albrecht&Cox Stds for PIR 38805

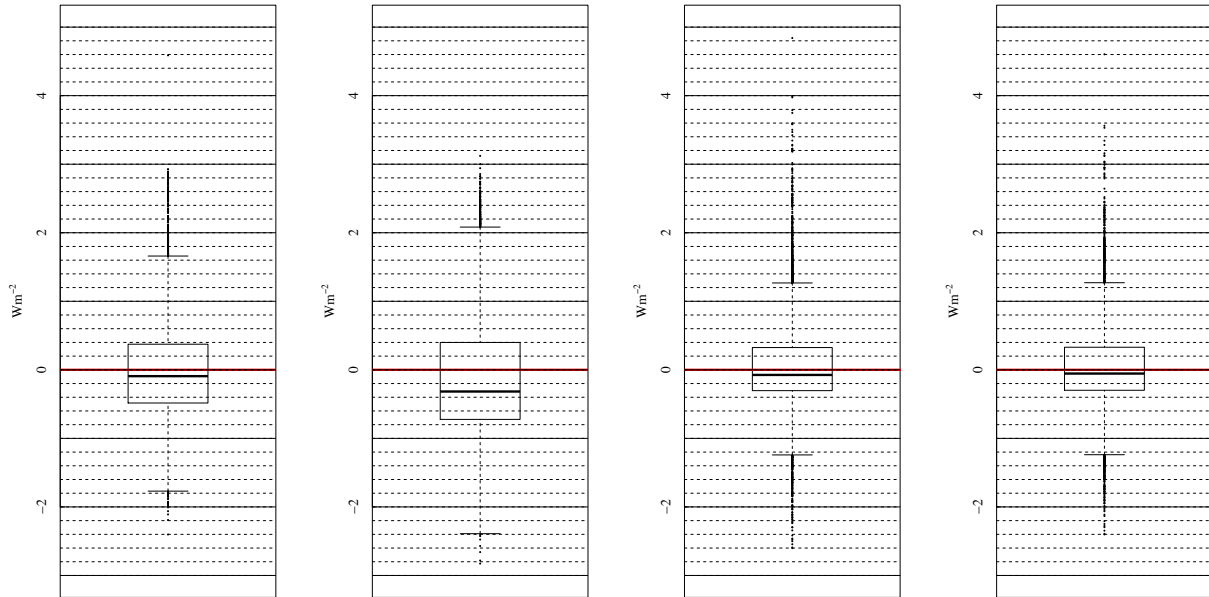
Philipona et al. Coefs, Philipona et al. Stds for PIR 38805



237
238 **Figure 4.** (top) Boxplots of the differences between applying Albrecht and Cox (1977)
239 calibrations and applying Philipona et al. (1995) calibrations for PIR 23215. Note the differences
240 in box widths, whisker lengths, and median values. (bottom) Boxplots for a different PIR
241 (38805) that was calibrated at the same time as the one in Fig. 4 (top).

242
243
244
245 Next, we compare results from all four equations (2), (3), (4), and (6) for the same two PIRs as in
246 Fig. 4. Since Fig. 4 suggests that the Philipona et al. (1995) Eq. (3) produces better results than
247 Albrecht and Cox (1977) Eq. (2), we use Philipona et al. (1995) coefficients provided by WRC
248 to compute IR irradiance for the standard PIRs and average these as “truth” for all of the
249 comparisons. For both test PIRs in Fig. 5 (top and bottom) the last boxplot on the right
250 (Philipona et al., 1995) gives the best results followed by the adjacent boxplot (Reda).
251
252

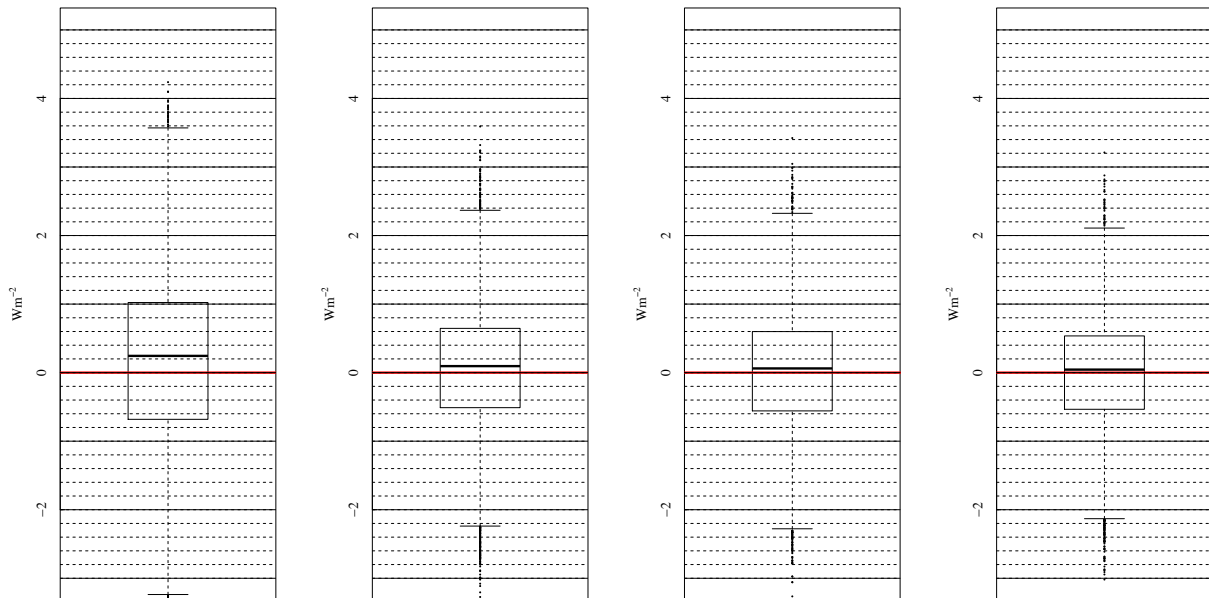
Left to Right, Albrecht Coefs, Payne Coefs, Reda Coefs, Philipona Coefs Using Philipona Stds for PIR 23215 2023 Cal



Albrecht = Albrecht and Cox (1977); Payne = Payne and Anderson (1999); Reda = Reda et al. (2002); Philipona = Philipona et al. (1995)

253

Left to Right, Albrecht Coefs, Payne Coefs, Reda Coefs, Philipona Coefs Using Philipona Stds for PIR 38805 2023 Cal



Albrecht = Albrecht and Cox (1977); Payne = Payne and Anderson (1999); Reda = Reda et al. (2002); Philipona = Philipona et al. (1995)

254

255

256 **Figure 5.** Boxplots of differences using the WRC’s Philipona et al. (1995) coefficients for the
 257 standard PIRs and calibrated PIRs to this standard using the four equations to calculate incoming
 258 IR. Top is for PIR 23215 and bottom is PIR 38805 as in Fig. 4. Compare box widths, whisker
 259 lengths, and medians.

260

261 In these comparison plots the standard used was calibrated with Philipona et al. (1995)
 262 coefficients rather than Albrecht and Cox (1977) as in Fig. 4. Similar results were obtained for

263 the other four PIRs with the best results always obtained with the Philipona et al. (1995)
264 formulation. In only one case out of the six the Payne and Anderson (1999) formula performed
265 slightly better than the Reda et al. (2002) formula (not shown).
266

267 T-tests were performed to assess differences when using non-Philipona et al. (1995) calibration
268 coefficients for all six calibrated instruments. If one assumes that there are no significant
269 differences in the calculation of IR irradiances using the Philipona et al. (1995) formula versus
270 each of the other three methods discussed, this assumption is rejected with 95% confidence in 15
271 of the 18 cases studied (six calibrated PIRs and three formulae). The three cases where the null
272 hypothesis cannot be rejected with 95% confidence are for three of the six PIRs using the Reda
273 et al. (2002) formula.
274

275 Reda et al. (2002) and Payne and Anderson (1999) did not use the measured body temperature
276 T_B in their formulae, but estimated the receiver temperature T_R using a form of Eq. (5) for their
277 particular PIR configuration. As a test we replaced T_B with T_R in the Philipona et al. (1995) Eq.
278 (3). The extremely small changes in the rightmost boxplots of Fig. 5 were imperceptible. We
279 would, therefore, suggest keeping Eq. 3 in its original form for calibration transfer.
280

281

282 **4. Precision of the PIR Standards**

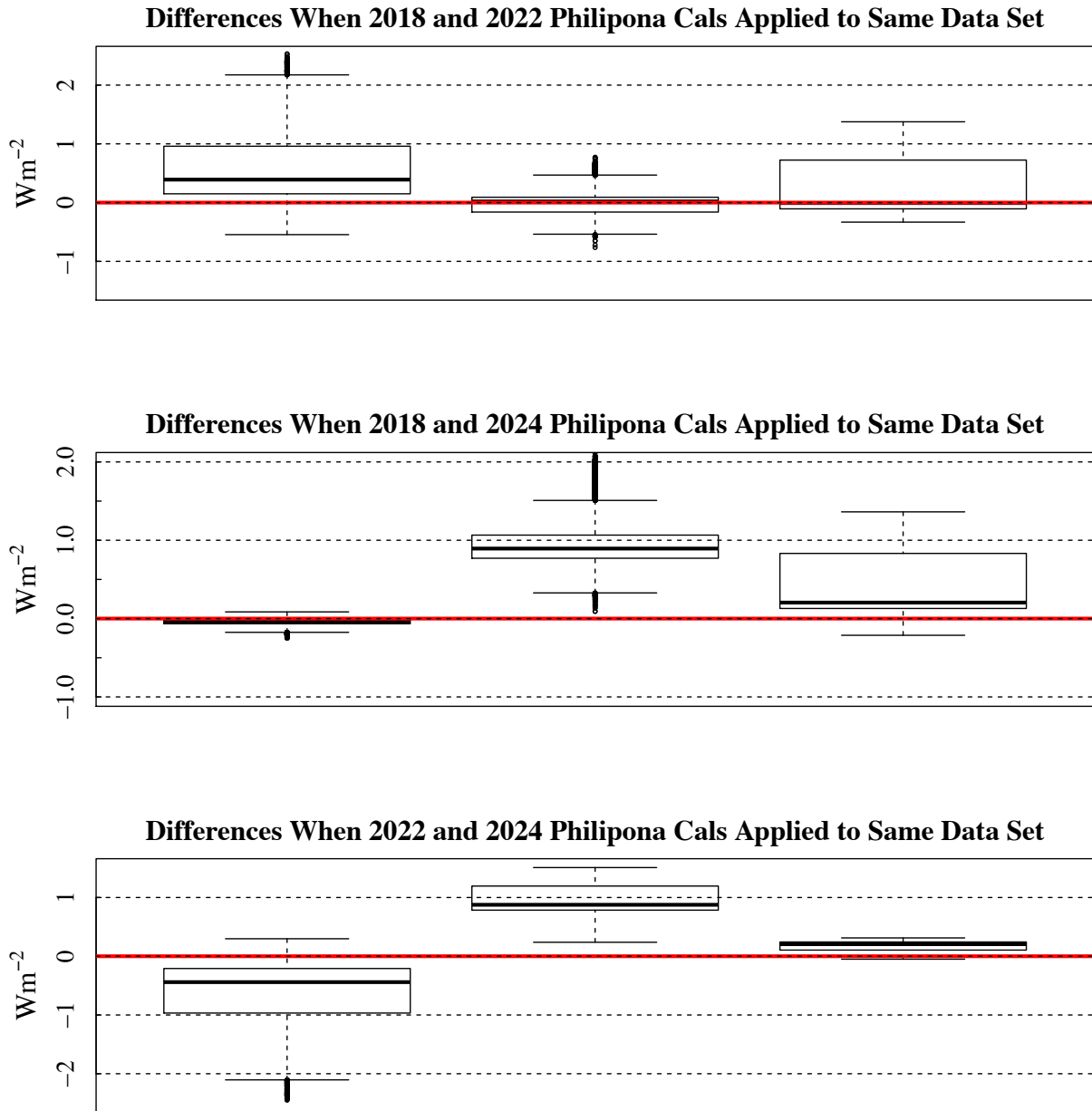
283

284 The calibration of our same three standard PIRs at the WRC leads to slightly different calibration
285 results. Here, the consistency and repeatability of those calibration events is assessed. The PIRs
286 that we use for standards were sent to WRC in 2018, 2022, and 2024. For each of those events,
287 coefficients for the Albrecht and Cox (1977) and Philipona et al. (1995) forms of the PIR
288 processing equation for calculating incoming IR were provided by the WRC.
289

290 Our calibration seasons typically run from late Spring to early Fall. Therefore, our three PIR
291 standard PIRs experience roughly six months of exposure to the weather each year. In Fig. 6
292 differences from applying three sets of WRC Philipona calibration coefficients (from 2018,
293 2022, and 2024) to the same dataset (that used for Fig. 3) are summarized. For example,
294 calibrations from 2018 and 2022 were applied to the same dataset and differences in irradiance
295 for each minute were tallied and summarized in boxplots. Differences for all permutations are
296 mostly within 1 Wm^{-2} and suggest that errors from applying one of the WRC calibrations from
297 any of the three calibration years to any year would be less than the uncertainty of the WRC
298 calibrations themselves ($\sim 4 \text{ Wm}^{-2}$; <https://www.pmodwrc.ch/en/?s=wisg>). This suggests that the
299 Eppley PIR is very stable and should be suitable for monitoring long-term changes in the thermal
300 IR.
301

301

302



Three Standards (31610, 32909, 32910) w/ WRC Cals from Three Different Years

303
 304 **Figure 6.** Comparisons of three sets of Philipona et al. (1995) calibration coefficients provided
 305 by the WRC in 2018, 2022, and 2024 applied to the same data set as in Fig. 3 for the three PIRs
 306 used as standard PIRs with serial numbers in the subtitle. The medians are all within 1 Wm^{-2} and
 307 most are within 0.5 Wm^{-2} .

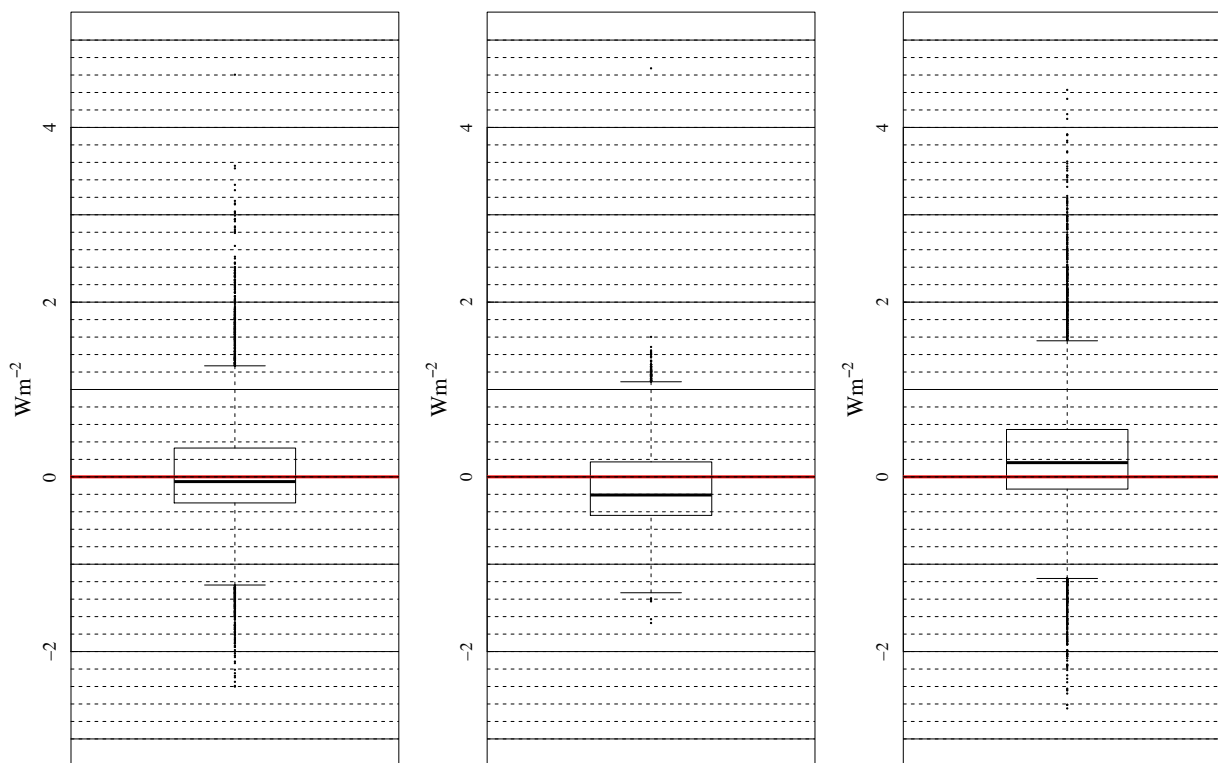
308
 309 In section 3 the average output of the three standard PIRs is used to derive new calibration
 310 coefficients for each test PIR. Using those new calibrations, the test instrument measurements
 311 are compared to the standard PIRs' average over the entire calibration period. For the left panels
 312 in Fig. 7 we use Philipona et al. (1995) coefficients for the standard PIRs to calibrate the three
 313 test PIRs (serial numbers shown at the top of each subplot). We apply those new calibrations and

314 subtract the results from the standard PIRs' average for each minute and summarize the
315 distribution of differences in boxplots. Therefore, the leftmost panels of Fig. 7 replicates the
316 rightmost panels of Figs. 4 and 5. This is not an independent test of the reliability of the
317 calibration because the same dataset is used for calibration and verification.

318
319 To test new calibrations with an independent dataset, the time series in Figure 3 is divided in
320 half. The middle panels of Fig. 7 use the first half of the data in Fig. 3 to derive a calibration and
321 the second half of the data to validate the new calibration against the standard PIRs' average.
322 Then, we reverse this process using the second half of the Fig. 3 data for calibrating and the first
323 half to validate. If we examine the time series in Fig. 3, it is apparent that the first half of the data
324 stream is noisier than the second half. Using the first half of the data to calibrate and applying to
325 the second half and vice versa is likely responsible for the offsets in the medians, but the offsets
326 are less than one Wm^{-2} . Note that when the less noisy data of the second half are used to validate
327 (middle boxplots) the differences have a smaller spread. When the noisier first half data
328 (rightmost boxplots) are used to validate, the differences have a larger spread. Examining the
329 top, middle, and bottom plots, there are differences inherent in the instruments themselves since
330 boxplots are not replicated from PIR to PIR. Attribution to the instruments themselves is
331 warranted because the standard PIRs and test data used for Fig. 7 were collected simultaneously.

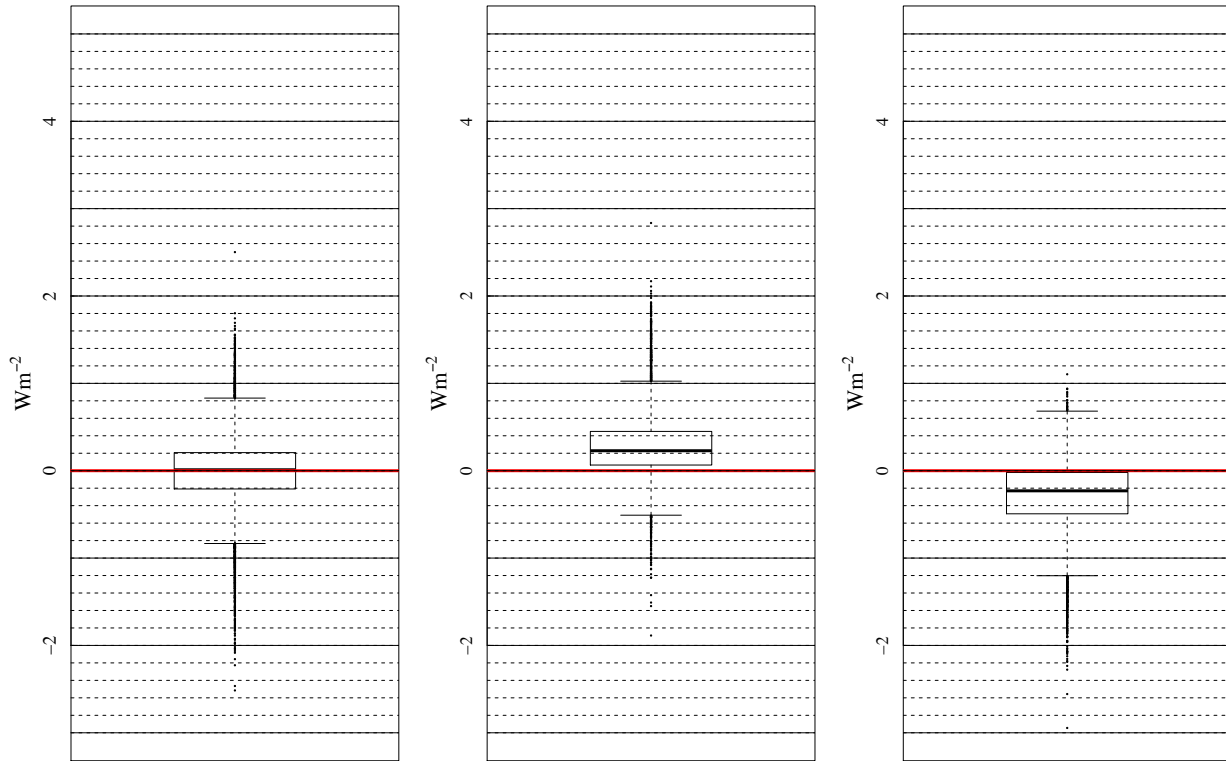
332

Left to Right: Full Cal Period; 1st Half Used for Cal, Applied to 2nd Half; and Vice Versa for PIR 23215



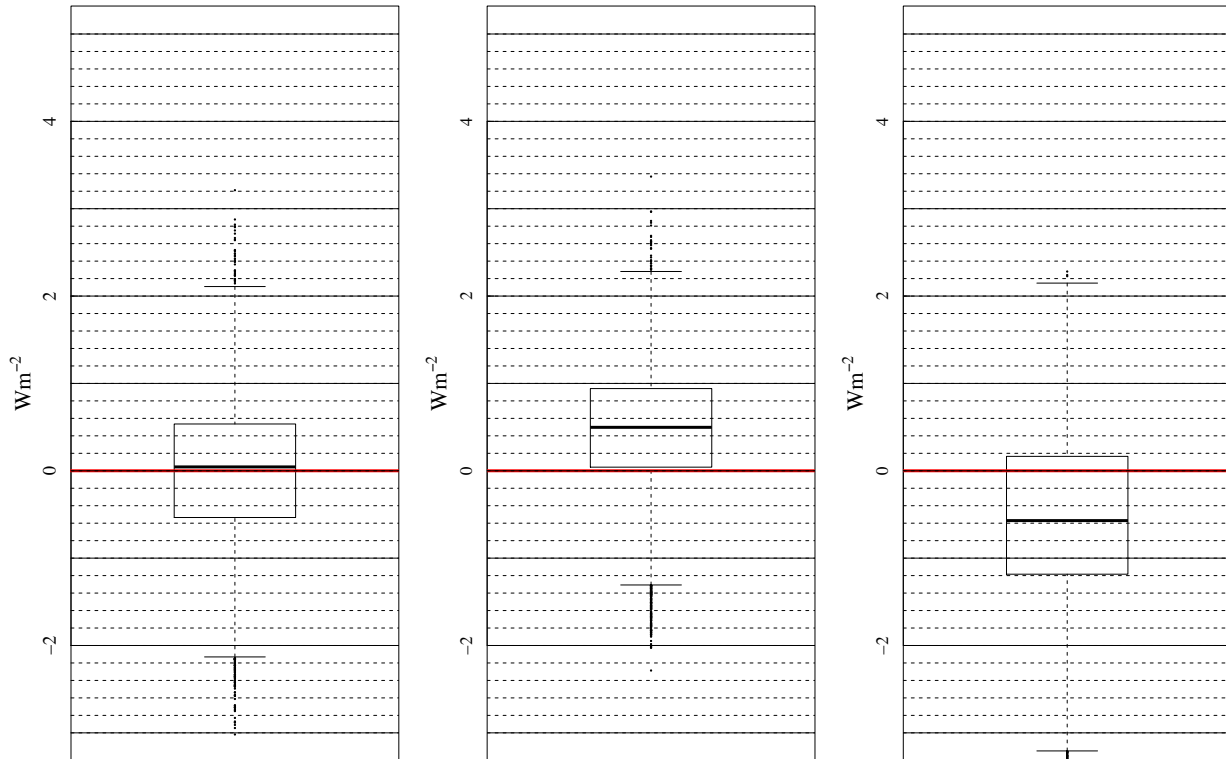
333

Left to Right: Full Cal Period; 1st Half Used for Cal, Applied to 2nd Half; and Vice Versa for PIR 28139



334

Left to Right: Full Cal Period; 1st Half Used for Cal, Applied to 2nd Half; and Vice Versa for PIR 38805



335

336 **Figure 7.** The leftmost panel uses the entire period in Fig. 3 to calibrate the named PIR and then
337 compares the calibrated PIR data to the standard PIRs' average. The middle panel uses the first
338 half of the period to calibrate and then assesses the application of those calibrations to an
339 independent data set in the second half. The rightmost panel reverses this using the second half
340 of the period for calibration and the first half for assessment.

341

342 **5. Summary and Conclusions**

343

344 In this paper we investigate four formulations for converting raw voltage and body and dome
345 temperature measurements of an Eppley pyrgeometer, model PIR, to thermal IR irradiance.
346 These methods are described in Albrecht and Cox (1977), Philipona et al. (1995), Reda et al.
347 (2002) and Payne and Anderson (1999). All are slight variations of the original formulation of
348 Albrecht and Cox (1977). Because the temperature measurements are critical to the infrared
349 calculations, we also investigated various fits that have been applied to the Steinhart-Hart (1968)
350 equation that converts thermistor-measured resistance to temperature.

351

352 Regarding the computation of thermistor temperatures, we found that fitting the manufacturer-
353 supplied table of resistance and temperature (1°C interval) to the range -50° to 50°C provides the
354 least variability as opposed to fits to shorter temperature ranges. However, differences of the fit
355 to the provided data are < 0.01°C, regardless of the range used. Based on this result, we conclude
356 that differences in thermistor temperature calculations from fits based on various temperature
357 ranges do not have a significant impact on PIR measurements.

358

359 The three standard PIRs that we use to transfer calibrations from the world standard to field PIRs
360 are calibrated frequently against the World Infrared Standard Group (WISG) at the World
361 Radiation Center in Davos, Switzerland. They are returned with calibration coefficients for the
362 Albrecht and Cox (1977) and Philipona (1995) methods, although the Albrecht and Cox
363 coefficients provided are for the shortened form of their equation (Eq. 2). Comparing the
364 application of the two methods to the standard PIRs revealed that the Philipona (1995) method is
365 more precise and less noisy than the Albrecht and Cox formulation; the differences are quantified
366 in Fig. 3(b) histograms. Comparisons were also made among three distinct WRC calibration
367 results for the standard PIRs in 2018, 2022, and 2024. They showed that the three standard PIRs
368 are stable, with the calibration coefficients changing minimally between WRC calibrations, and
369 differences in irradiance calculations among applications of the separate biennial calibrations are
370 within one Wm^{-2} of each other.

371

372 Application of the four methods for converting PIR raw measurements to irradiance was
373 analyzed using six test instruments. The major conclusion is that use of the Philipona et al.
374 (1995) form, i.e., Eq. (3), consistently does the best in transferring the mean calibration of the
375 standard PIRs to field-deployed PIRs. Note that Reda et al. (2002) and Payne and Anderson
376 (1999) coefficients are not available for the standard PIRs calibrated at the WRC, which may
377 have led to some of the differences in Fig. 5. Of the six calibration comparisons, like those in
378 Fig. 5, Reda et al. (2002) calibration results were close to Philipona et al. (1995) results on three
379 of the six PIRs according to t-tests performed at the 95% level. However, this agreement was
380 found to be insignificant for the t-tests on the other three PIRs.

381

382 Given the differences in Figs. 6 and 7, it is probable that there is greater uncertainty caused by
 383 the particular atmospheric conditions under which calibrations are carried out. With the
 384 assumption that the PIR is very stable, the variations among the instruments in Fig. 6 could be
 385 subtle differences in atmospheric conditions during the three calibration sessions at the WRC in
 386 2018, 2022, and 2024. This is reinforced by the differences in Fig. 7, where independent stable
 387 (i.e., clear), and unstable (e.g., intermittent clouds) periods were used to calibrate test
 388 instruments, with differing results. Note that PIR measurements for any arbitrary weather
 389 condition are often going to have larger uncertainties than discussed here.
 390

391 The WISG, which is used for calibration at the WRC, is the current standard for broadband IR
 392 measurements. It has an uncertainty of 2.6 Wm^{-2} . Recent studies, which are summarized in
 393 Gröbner et al. (2024), further suggest that the current WISG may be low by as much as 4 Wm^{-2} if
 394 the water vapor column exceeds 1 cm, but the difference is smaller if the atmosphere is dryer
 395 approaching no difference for vanishing water vapor (see Fig. 2 in Gröbner et al., 2024).
 396 Nevertheless, a new standard for broadband IR radiation is not expected to be established until
 397 the next WMO congress in 2027 at the very earliest (Laurent Vuilleumier, private
 398 communication).

399
 400

401 **Appendix A1**

402

403 Fitting the manufacturer-supplied temperature (at $1 \text{ }^\circ\text{C}$ intervals) and resistance data, separately
 404 in ohms and in kilohms, led to an unexpected outcome. First, if a full cubic (i.e., non-zero
 405 coefficient for the squared term) least-squares fit of the Steinhart-Hart equation with YSI 44031
 406 data in kilohms is compared to a least-squares fit using ohms, identical fits are obtained (blue
 407 and white dashed line in Fig. 2). If the quadratic term is set to zero and the fits are made to ohms
 408 and then kilohms, we see a significant difference as shown in Fig. A1. This difference is due to
 409 numerical reasons, which are explained in the following.

410

411 First, it must be noted that the lack of significant digits when using kilohms is not an issue
 412 because for the fits here, kilohms are computed simply by dividing the resistance value in ohms
 413 by 1000, keeping significant digits in the decimal places.

414

415 The requirement of a quadratic term for expressing the Steinhart-Hart equation in kilohms can
 416 be demonstrated by substituting for R in Eq. (7) $1000R_k$, where R_k is in units of kilohms as
 417 shown in Eq. (A1).

418

$$419 \quad \frac{1}{T} = a + b \cdot \ln(1000R_k) + d \cdot \ln(1000R_k)^3 \quad (\text{A1})$$

420

421 Applying logarithm rules to Eq. (A1) results in Eq. (A2).

422

$$423 \quad \frac{1}{T} = a + b(\ln(1000) + \ln(R_k)) + d(\ln(1000) + \ln(R_k))^3 \quad (\text{A2})$$

424

425 Expanding and regrouping terms in Eq. (A2) then gives Eq. (A3) through Eq. (A7).

426
 427
 428
 429
 430
 431
 432
 433
 434
 435
 436
 437
 438
 439
 440
 441
 442
 443
 444
 445
 446
 447

$$\frac{1}{T} = a_k + b_k \cdot \ln(R_k) + c_k \cdot \ln(R_k)^2 + d_k \cdot \ln(R_k)^3 \quad (\text{A3})$$

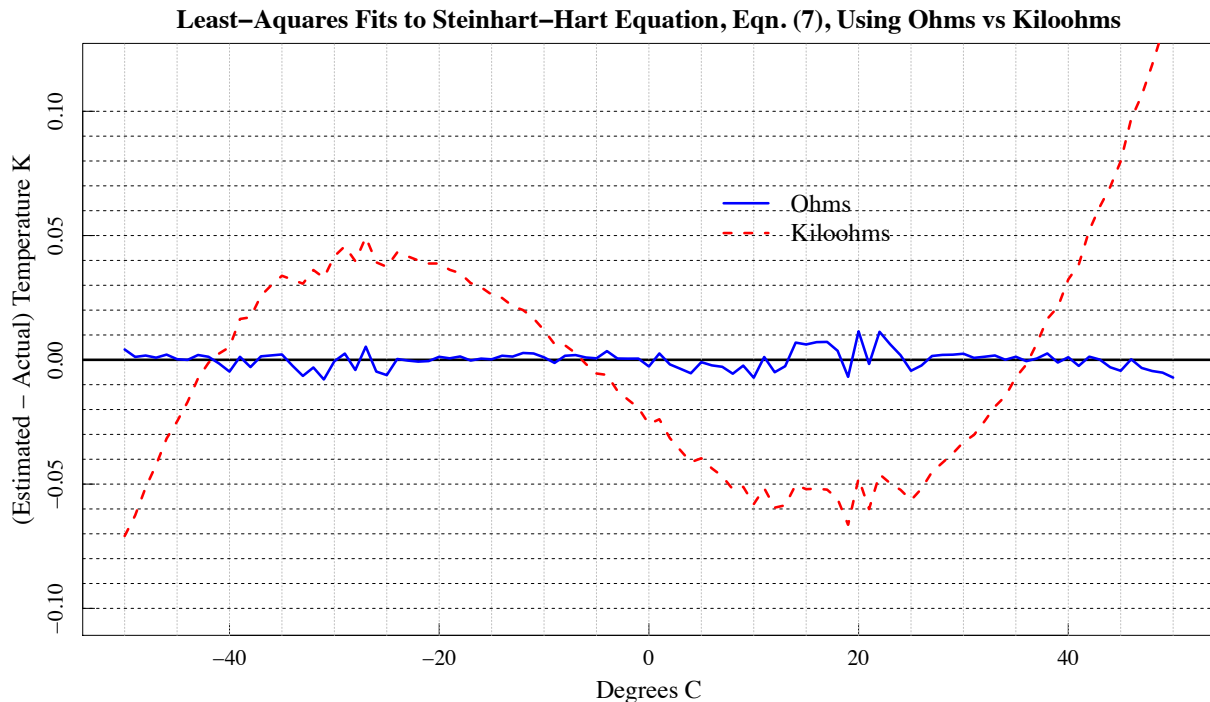
$$a_k = a + b \cdot \ln(1000) + d \cdot \ln(1000)^3 \quad (\text{A4})$$

$$b_k = b + 3d \cdot \ln(1000)^2 \quad (\text{A5})$$

$$c_k = 3d \cdot \ln(1000) \quad (\text{A6})$$

$$d_k = d \quad (\text{A7})$$

Thus, when data are in kilohms an equation of the form of Eq. (A3) (i.e. full cubic) is required to match the results of Eq. (7) when data are in units of ohms. Thus, changing units of R in Eq. (7) results in a full cubic equation. This implies that a full cubic equation can be more robust than Eq. (7) when fitting data where units other than ohms are used for R . It also demonstrates that it is possible to change units for R in Eq. (7) analytically using the substitution process shown above rather than refitting if desired.



448
 449
 450
 451
 452

Figure A1. Steinhart-Hart equation (i.e., no quadratic term) fit to ohms (blue solid line) versus kilohms (red dashed line).

453 *Code availability.* Codes used to generate the results in this paper were original functions written in the
454 programming language R and are available by contacting joseph.michalsky@noaa.gov.

455 *Data availability.* Data can be made available by contacting joseph.michalsky@noaa.gov.

456 *Author contributions.* JJM did most of the analyses, drafted the paper, and produced the figures. JAA
457 provided the World Radiation Center calibrations and much useful discussion of the results. EH provided
458 the experimental data from the calibration table used for these analyses. BRS did the analysis for and
459 wrote the Appendix. All authors read and offered corrections to parts of the manuscript.

460

461 *Competing interests.* The contact author has declared that none of the authors has any competing interests.

462

463 *Acknowledgments.* The authors would like to thank Kathy Lantz for a careful reading of this paper.
464 Christopher Cox and another reviewer, who wished to remain anonymous, refereed the paper that
465 substantially improved the final result. Julian Groebner added useful information in a community
466 comment. Bruce Forgan privately sent comments on the paper that were appreciated.

467

468 *Financial support.* This research has been supported by the Global Monitoring Laboratory of the National
469 Oceanic and Atmospheric Administration.

470

471

472

473

474

475 **References**

476

477 Albrecht, B. and Cox, S. K.: Procedures for improving pyrgeometer performance, *J. Appl.*
478 *Meteorol.*, 16, 188-197, [https://doi.org/10.1175/1520-0450\(1977\)016<0190:PFIPP>2.0.CO;2](https://doi.org/10.1175/1520-0450(1977)016<0190:PFIPP>2.0.CO;2),
479 1977.

480 Gröbner, Julian, Thomann, Christian, Reda, Ibrahim, Turner, David D., Feierabend, Moritz,
481 Monte, Christian, McComiskey, Allison, and Reiniger, Max: Traceability of surface longwave
482 irradiance measurements to SI using the IRIS radiometers, *AIP Conference Proceedings*, 2988,
483 070001, <https://doi.org/10.1063/5.0183304>, 2024.

484 McArthur, L.: Baseline Surface Radiation Network (BSRN) - Operation Manual Version 2.1,
485 Ontario, Canada, WMO, p. 68, [hdl:10013/epic.52032](https://hdl.handle.net/10013/epic.52032), 2005.

- 486 Payne, R.E. and Anderson, S.P.: A new look at calibration and use of Eppley precision infrared
487 radiometers. Part II: calibration and use of the woods hole oceanographic institution improved
488 meteorology precision infrared radiometer, J. Atmos. Ocean. Tech., 16, 741-751,
489 [https://doi.org/10.1175/1520-0426\(1999\)016<0739:ANLACA>2.0.CO;2](https://doi.org/10.1175/1520-0426(1999)016<0739:ANLACA>2.0.CO;2), 1999.
- 490 Philipona, R., Frohlich, C., and Betz, C.: Characterization of pyrgeometers and the accuracy of
491 atmospheric longwave, Appl. Optics, 34, 1598-1605, <https://doi.org/10.1364/AO.34.001598>,
492 1995.
- 493
494 Reda, Ibrahim, Hickey, John R., Stoffel, Tom, and Myers, Daryl: Pyrgeometer calibration at the
495 National Renewable Energy Laboratory (NREL), J. Atmos. Sol.-Terr. Phy., 64, 1623-1629,
496 [10.1016/S1364-6826\(02\)00133-5](https://doi.org/10.1016/S1364-6826(02)00133-5), 2002.
- 497 Steinhart, John S. and Hart, Stanley R.: Calibration curves for thermistors, Deep-Sea Res., 15,
498 497-503, [https://doi.org/10.1016/0011-7471\(68\)90057-0](https://doi.org/10.1016/0011-7471(68)90057-0), 1968.